

# Large Eddy Simulation of Turbine Internal Cooling Ducts

J. Tyacke<sup>a,\*</sup>, P. G. Tucker<sup>a</sup>,

<sup>a</sup>*Whittle Laboratory, Department of Engineering, University of Cambridge, Cambridge, UK*

---

## Abstract

Large-Eddy Simulation (LES) and hybrid Reynolds-averaged Navier-Stokes-LES (RANS-LES) methods are applied to a turbine blade ribbed internal duct with a 180 degree bend containing 24 pairs of ribs. Flow and heat transfer predictions are compared with experimental data and found to be in agreement. The choice of LES model is found to be of minor importance as the flow is dominated by large geometric scale structures. This is in contrast to several linear and nonlinear RANS models, which display turbulence model sensitivity. For LES, the influence of inlet turbulence is also tested and has a minor impact due to the strong turbulence generated by the ribs. Large scale turbulent motions destroy any classical boundary layer reducing near wall grid requirements. The wake-type flow structure makes this and similar flows nearly Reynolds number independent, allowing a range of flows to be studied at similar cost. Hence LES is a relatively cheap method for obtaining accurate heat transfer predictions in these types of flows.

*Keywords:* LES, Turbine, Heat transfer, RANS, SGS

---

## Nomenclature

		$Pr$	Prandtl number
$C$	Model constant	$Re$	Reynolds number
$D$	Duct height	$T$	Temperature, K
$P$	Turbulence production	$\dot{m}$	Mass flowrate, kg/s
		$\mathbf{x}$	Coordinate direction
		$\tilde{d}$	Modified wall distance

---

\*Corresponding author

*Email address:* jct53@cam.ac.uk (J. Tyacke)

$d$	Wall distance
$h$	Rib height
$k$	Turbulent kinetic energy
$l$	Length scale
$t$	Time
$u, v, w$	Cartesian velocity components, m/s
$y^+$	Wall distance in wall units
$ave$	Average
$i$	Component
$in$	Inlet
$L, \alpha, K$	Leray, $\alpha$ , Kosović
$T$	Turbulent
$x, ax$	Axial
CD	Central difference
$\varepsilon$	Turbulence dissipation rate

## 1. Introduction

In gas turbines, high pressure turbine blades operate in an environment where gas temperatures are significantly higher than the safe operating temperature of the metal. This harsh environment requires the blade

to be adequately cooled to prevent premature wear or failure. Hence, to continue to make improvements in efficiency and lifespan, reliable predictive technology is of great importance. Internal cooling passages are used to reduce metal temperatures and often incorporate ribs and other intricate structures to increase turbulence and hence heat transfer within such ducts. A schematic indicating turbine blade internal cooling ducts and an idealised geometry is provided in Fig. 1. In this figure, serpentine passages (passages with 180 degree bends) containing ribs are visible. It is well known that such flows challenge turbulence models.

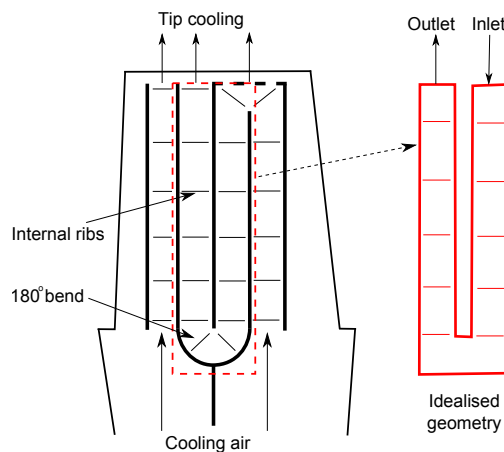


Figure 1: Schematic showing turbine blade internal cooling ducts with rib turbulators and the idealised geometry.

Turbulence modelling in industry is domi-

nated by the use of RANS models, which are often poor at predicting both the flow and heat transfer in complex geometries with separated flow. For example, Ooi et al. [1] study cooling passage heat transfer using the  $v^2-f$ ,  $k-\varepsilon$  and Spalart-Allmaras RANS model. Secondary flow structures are found not to be modelled well using the eddy viscosity concept. In some cases, differences between other RANS models varies by approximately 100% [2].

Saha and Acharya [3] contrast unsteady-URANS (URANS) ( $k - \varepsilon$  model) and LES (Dynamic Smagorinsky model [4]) approaches to model rotating and non-rotating ribbed ducts. Tafti [5] studies a periodic ribbed duct section using quasi-DNS (quasi-Direct Numerical Simulation) and LES using the Dynamic Smagorinsky model. Both quasi-DNS and LES were found to be within 10-15% of each other and within 15-30% of experimental data dependent on mesh resolution. Sewall et al. [6] investigate flow and heat transfer in the developing, fully developed, and bend regions of a ribbed duct with a 180 degree bend. LES matches with mean velocity, Reynolds stresses and heat transfer measurements to within 10–15%. Viswanathan and Tafti [7]

compare LES and Detached Eddy Simulation (DES) [8] (LES with an extensive near wall RANS region) in the same ribbed duct. DES was found to improve predictions over the RANS. It did not however capture shear layer transition accurately, predicting a development length around two rib pitches greater than the LES. Ramgadia and Saha [9] use LES to study a periodically repeating ribbed duct section. A shear-improved Smagorinsky model is used, with LES data agreeing with measurements.

The above has shown that relative to RANS, LES is promising. This is especially so for this type of flow. For example, the often cited limitation of LES is the extreme increase in grid count with Reynolds number ( $\approx Re^{2.5}$  [10]). As noted by [11, 12, 13], ribbed passage flows are Reynolds number independent. They are governed by large scales of turbulence, of the order of the rib height. Hence, in this paper, we seek to explore the benefits of LES relative to RANS. In the above, the range of LES models evaluated and strategies considered was limited. Hence, here we seek to contrast a range of LES models. These include Numerical-LES (NLES), hybrid RANS-NLES and linear and nonlinear LES subgrid scale (SGS)

models. We also note that inflow sensitivity has not been fully explored. To this end, we bracket a measured 2% intensity with an extreme range of intensities to study this aspect.

The paper is set out as follows. The problem definition, governing equations and numerical details are presented. The turbulence modelling section then introduces the SGS and hybrid RANS-NLES models used and inflow conditions. The results section then discusses flow and turbulence statistics, in addition to heat transfer, before conclusions are drawn.

## 2. Problem Definition

The ribbed passage studied is shown in Fig. 2 and is consistent with that of [7]. The duct, comprising of an inlet and outlet leg connected with a  $180^\circ$  section includes 24 pairs of ribs on the top and bottom surfaces. Every surface is maintained at an arbitrary temperature of 294 K with the inlet air temperature fixed at 274 K. The duct inlet,  $180^\circ$  bend and outlet legs have a cross section of  $D \times D$ , where  $D=0.149$  m. The ribs have a width  $\times$  height  $\times$  length of  $h \times h \times D$ , where  $h = 0.1D$ . The pitch  $P$ , between ribs as marked with dotted lines in Fig.

2, is equal to  $D$  and each pair of ribs are aligned vertically. The width of the central divider is  $0.5D$ . The Reynolds number  $Re = 20,000$  is based on the bulk velocity  $U_0$  and  $D$ . A schematic of the geometry (not to scale) is shown in Fig. 3.

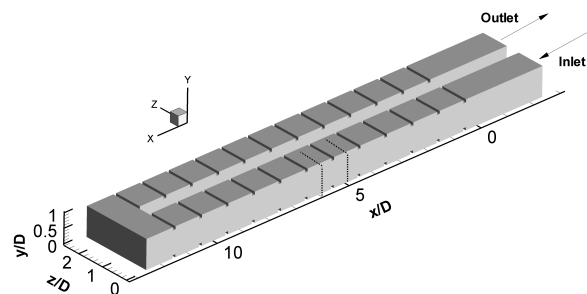


Figure 2: Ribbed passage geometry.

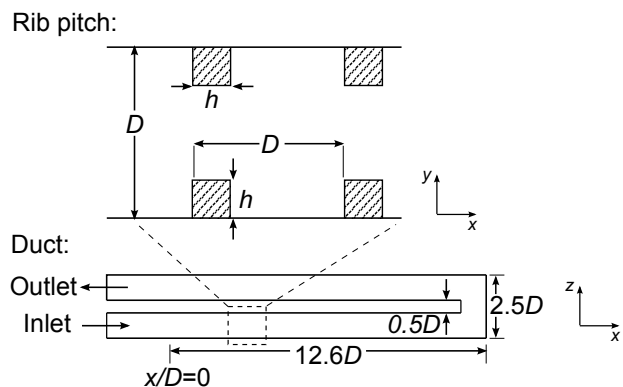


Figure 3: Geometry schematic showing one rib pitch and the complete duct (not to scale).

## 3. Governing Equations

The incompressible governing equations for (U)RANS/LES are based on the weakly

conservative form of the Navier-Stokes equations as in Eq. 1 and 2, the temperature equation given in Eq. 3. The tilde ( ) symbol represents either RANS or LES variables in these equations. The key difference between typical (U)RANS and LES is the averaging in time to obtain the (U)RANS equations and spatial filtering to obtain the LES equations. Both methods are explained in detail by Pope [14]. For (U)RANS, variables are split into a time mean and mean fluctuating component. For LES, the spatial filtering results in large resolved filtered scales and sub-grid scales which are not resolved. These time-average and filtering operations (represented by the tilde symbol) give rise to the need to close the set of equations by modelling the Reynolds or subgrid scale (SGS) stress tensor respectively. This is denoted by  $\tau_{ij}$  in Eq. (2). For the temperature equation, the heat flux tensor  $h_j$  is also modelled. For linear turbulence models, only the eddy viscosity  $\mu_T$  requires calculation, for non-linear models additional terms are added to  $\tau_{ij}$ .

$$\frac{\partial \tilde{u}_j}{\partial x_j} = 0 \quad (1)$$

$$\begin{aligned} \rho \frac{\partial \tilde{u}_i}{\partial t} + \rho \frac{\partial (\tilde{u}_i \tilde{u}_j)}{\partial x_j} &= - \frac{\partial \tilde{p}}{\partial x_i} \\ &+ \frac{\partial}{\partial x_j} \left[ \mu \frac{\partial \tilde{u}_i}{\partial x_j} \right] - \frac{\partial \tau_{ij}}{\partial x_j} \end{aligned} \quad (2)$$

$$\rho \frac{\partial \tilde{T}}{\partial t} + \rho \frac{\partial (\tilde{u}_j \tilde{T})}{\partial x_j} = + \frac{\partial}{\partial x_j} \left[ \frac{\mu}{Pr} \frac{\partial \tilde{T}}{\partial x_j} \right] - \frac{\partial h_j}{\partial x_j} \quad (3)$$

## 4. Numerical Details

### 4.1. Solver details

The solver used is a modified version of the NEAT code as provided by Tucker [15]. This is an incompressible finite volume code using a staggered grid and the SIMPLE scheme to couple velocity and pressure [16]. Second order central differences are used for the calculation of fluxes and the time scheme used is that of Crank-Nicolson. In previous studies on similar geometries [2], no higher order flux calculations provided consistently improved results. OpenMP is used to parallelise the code. The code has previously been verified and used to study similar geometries [17].

### 4.2. Resolution

To remain consistent, all simulations presented are run with a grid of  $982 \times 92 \times 117$

resulting in approximately 7 million internal nodes. First off wall grid spacings were set to  $0.01h$  giving a  $\Delta y^+$  value less than 1. Along each side of each rib, 26 nodes are used, with 60 between streamwise rib pairs and 43 between vertical rib pairs. As shown in Fig. 4, the grid is stretched towards walls to resolve high near wall gradients. Due to the large scale separation and reattachment in the flow, no significant fine near wall structures develop. The grid used was acceptable for LES [2], hence more than adequate for the RANS layer in the hybrid RANS-NLES. Where no significant classical boundary layer content exists, it has previously been shown that (N)LES is fairly insensitive [2].

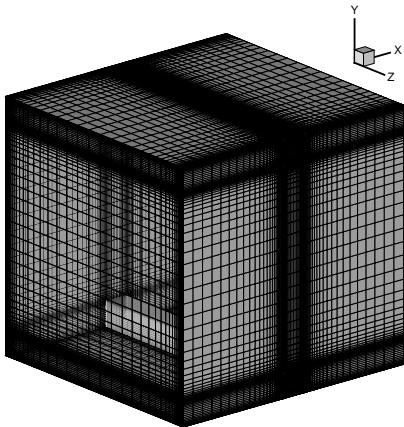


Figure 4: Grid for a single rib pitch.

All unsteady calculations ((N)LES and

hybrid RANS-NLES) were run for  $25t^*$  to develop the flow and temperature fields, then time averaged for the same period. Here, the non-dimensional time-scale  $t^*$  is defined using the bulk axial velocity and  $D$ . The CFL number was kept below 0.5 throughout the whole flow. The total computational cost was approximately 30,000 core hours including initial transients, running in parallel using 8 core AMD Opteron 2.6GHz processors. Using more efficient parallelisation, a simulation could be run in under 2.5 days using 500 cores on a modest compute cluster.

#### 4.3. Heat transfer data reduction

To study heat transfer, the ratio of the local Nusselt number  $Nu$  and the smooth duct Nusselt number  $Nu_0$ , is used. The Dittus-Boelter correlation defines  $Nu_0 = 0.023Re^{0.8}Pr^{0.4}$ , where  $Pr = 0.7$  for air. As [18],  $Nu$  is calculated using  $Nu = 1/(\theta_s - \theta_{ref})$ , where the non-dimensional temperature,  $\theta = (T - T_{in})/(q''D/k)$ . The wall heat flux, thermal conductivity, local and inlet temperature and surface indicator are represented as  $q''$ ,  $k$ ,  $T$ ,  $T_{in}$  and  $s$  respectively. The reference temperature,  $\theta_{ref}$  provides a local bulk mean temperature at an  $x$ -plane

in the inlet leg of the duct as Eq. 4.  $\theta$  is calculated using the local temperature  $T$ , and  $\theta_s$ , the local surface temperature  $T_s$ .

$$\theta_{ref} = \left( \iint_{A_x} |u| \theta dA_x \right) / \left( \iint_{A_x} |u| dA_x \right) \quad (4)$$

## 5. Turbulence Modelling

### 5.0.1. Yoshizawa $k-l$

As previously stated, the turbulent stress tensor  $\tau_{ij} = L + NL$  requires modelling and consists of a linear ( $L$ ) and nonlinear ( $NL$ ) part. For linear eddy viscosity based models,  $NL = 0$  and  $L = \tau_{kk}\delta_{ij}/3 - 2\mu_T S_{ij}$ , where  $S_{ij}$  is the strain rate tensor. The slightly modified model of Yoshizawa [19] is used as described in [20]. This gives a linear and purely dissipative SGS model that introduces history and non-local effects by use of an extra transport equation for the turbulent kinetic energy  $k_T$ . Basing the turbulent viscosity on the kinetic energy gives the isotropic relation  $\mu_T = \rho C_\mu l_\mu k_T^{1/2}$ . Hence, based on  $k_T$ , the eddy viscosity tends to zero near walls. The turbulence production and dissipation terms are given below by Eqs. (5) and (6) respectively. The turbulent

Schmidt number for kinetic energy,  $\sigma_k = 1$  [14].

$$P_{k_T} = 2 \frac{\mu_T}{\rho} \overline{S_{ij} S_{ij}} \quad (5)$$

$$\varepsilon_T = C_\varepsilon k_T^{3/2} / l_\varepsilon \quad (6)$$

Because this model is similar in form to the RANS model of Wolfshtein [21], only the length scales and constants need to be changed. The LES length scales for this  $k-l$  based model are given by  $l_{\varepsilon,LES} = l_{\mu,LES} = \Delta$ . This relates the smallest resolved scales with the largest unresolved scales, with the constants  $C_\varepsilon = 1.05$  and  $C_\mu = 0.07$ . The minimum of the RANS (see later) and LES length scales are taken to produce a smooth transition of  $\mu_T$  in the near wall region. When referring to this model in the results, the label *Yosh.* will be used.

### 5.1. Mixed nonlinear models

Nonlinear models are potentially better able to model the anisotropy found in shear flows. However, on their own, these models do not generally dissipate enough energy from the flow, which can cause solution instability. To remedy this, here, a mixed form is chosen in which dissipation is achieved using the linear Yoshizawa

model to calculate  $\mu_T$ . Other nonlinear terms are then added via source terms to provide a more advanced SGS model. Modelling turbulence anisotropy may be beneficial when using coarser grids, although nonlinear models are also more sensitive to numerical dissipation. Nonlinear SGS models are also able to model local energy backscatter from the small scales to the larger scales. This may occur where large coherent structures develop in the flow field and has been confirmed using DNS [22].

Of the models studied here, two are based on the concept of regularisation of the Navier-Stokes equations. This may be interpreted as a smoothing operation and can be cast in the LES context. The Leray model is based on a *smoothed transport velocity* whereas the LANS- $\alpha$  formulation is created from the *filtered Kelvin circulation theorem* which incorporates the smoothed transport velocity. The third nonlinear model considered is that of Kosović, which is a phenomenological model.

For each mixed nonlinear SGS model, the nonlinear terms  $NL$  are provided in Tab. 1, where  $\alpha = \Delta$  and  $C$  represents a constant. The comma separated indices represent derivatives, repeated indices indi-

cating summation. When calculating  $\mu_T$ ,  $C_\mu = 0.05$ . The magnitude of the additional nonlinear terms ( $NL$ ) are limited to the magnitude of the linear terms ( $L$ ). This is done for all the mixed nonlinear models applied and ensures numerical stability. Since the Taylor expansion at quadratic order of the box and Gaussian filters is the same [23, 24], the velocities for the nonlinear term are smoothed using a second order approximation to the Gaussian filter and the resolved variables are grid filtered. When referring to these models in the results, the labels *Ler.*, *Alp.* and *Kos.* will be used for Leray, Alpha and Kosović respectively.

Table 1: Nonlinear LES model terms.

Model	$NL$ (additional nonlinear terms)
Yoshizawa	-
Leray	$C_L \rho \alpha^2 [u_{i,k} u_{k,j} + u_{i,k} u_{j,k}]$
$\alpha$	$C_\alpha \rho \alpha^2 [u_{i,k} u_{k,j} + u_{i,k} u_{j,k} - u_{k,i} u_{k,j}]$
Kosović	$C_K \rho \alpha^2 [u_{i,k} u_{k,j} + 3u_{i,k} u_{j,k} - u_{k,i} u_{k,j}]$

## 5.2. Numerical-LES

The Numerical-LES (NLES) scheme uses no explicit SGS model. Instead it relies upon dissipation resulting from the numerical scheme to remove energy. For example, a second order solver will produce terms of

a similar form to the Smagorinsky model [25] due to terms of the order  $\Delta^2$ . The implied subgrid model is hence, determined by the structure of the resolved flow [26] and the numerical aspects of the solver. Specially designed numerical schemes can be formulated to give more formal closures [27], though here, no claims are made about the quality of the resulting implied model.

### 5.3. *k-l based RANS-NLES*

A technique commonly employed to reduce near wall grid requirements, especially for high Reynolds numbers, is to use a hybrid RANS-(N)LES model. Although little classical boundary layer is expected and the Reynolds number is low, it seems informative to apply the strategy. To model any near wall streaks in the hybrid RANS-NLES simulation, the Wolfshtein [21]  $k-l$  RANS model is employed. To calculate the eddy viscosity for this model, an equation for the kinetic energy is solved and the turbulent viscosity is then given by  $\mu_T = \rho C_\mu l_\mu k^{1/2}$ . The constants are defined as  $C_\varepsilon=1$  and  $C_\mu=0.09$  and the RANS length scales are given by  $l_{\varepsilon,RANS} = 2.4y(1 - e^{-0.263y^*})$  and  $l_{\mu,RANS} = 2.4y(1 - e^{-0.016y^*})$ , where  $y^* = y\rho k_T^{1/2}/\mu$ . For the NLES region, the turbu-

lent viscosity is brought to zero by modifying the length scales via the wall distance. The interface is located at  $d = 0.1h$ .

To provide a smooth transition from the RANS to NLES regions, the true wall distance is modified using a Hamilton-Jacobi equation. This is shown in Eq. (7).

$$|\nabla \tilde{d}| = 1 + f(\tilde{d})\nabla^2 \tilde{d} + g(d) \quad (7)$$

The RANS wall distance is replaced with the modified wall distance. This retains accurate wall distances nearest the wall, then smoothly returns the wall distance to zero for the NLES region. Further smoothing is hence not required. Figure 5 displays the modified wall distance and the resulting RANS and NLES regions.

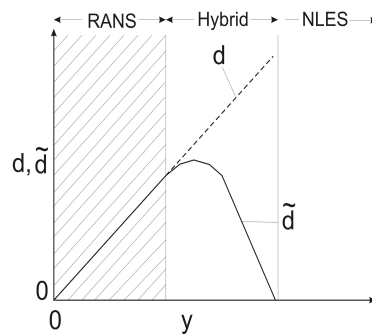


Figure 5: Wall distance/blending function from the Hamilton-Jacobi equation.

The technique is described in detail in [28]. When referring to this model in the results, the label *RANS-NLES* will be used.

#### 5.4. Thermal modelling

For all computations the eddy diffusivity model below is used. For LES regions the turbulent Prandtl number  $Pr_T = 0.4$  [29] and for RANS  $Pr = 0.9$  [30, 31]<sup>1</sup>.

$$h_j = -\frac{\mu_T}{Pr_T} \frac{\partial \tilde{T}}{\partial x_j} \quad (8)$$

Similarly to the the addition of the eddy viscosity to obtain an effective viscosity to model the stress tensor, the effective thermal diffusivity is then obtained

$$\Gamma = \frac{\mu}{Pr} + \frac{\mu_T}{Pr_T} \quad (9)$$

#### 5.5. Turbulent inflow

To represent true running conditions, LES should typically encompass as much available data as possible. To assess the impact of imposed turbulence at the inlet, turbulent fluctuations were applied at the inlet of one LES (Alp.+Inlet) by running a precursor periodic duct simulation. The same grid is used in the  $y - z$  plane with a duct that is  $6D$  long and periodic in  $x$ . The mass flowrate is matched to that of the cooling duct by adjusting the pressure gradient. The velocity fluctuations of 10%

<sup>1</sup>In future, the use of a variable  $Pr_T$  may offer some benefit.

turbulence intensity are added to the mean velocity profiles of Graham et al. [32]. In the experiment, these were designed to be nearly uniform, with a low turbulence intensity of 2%. Hence the LES, with and without inlet turbulence, provides a contrast. At each time step, the resulting velocities are imposed  $0.24D$  upstream of the first rib. This provides physically realistic turbulence at the inlet. Figure 6 provides contours of instantaneous axial velocity at the inlet.

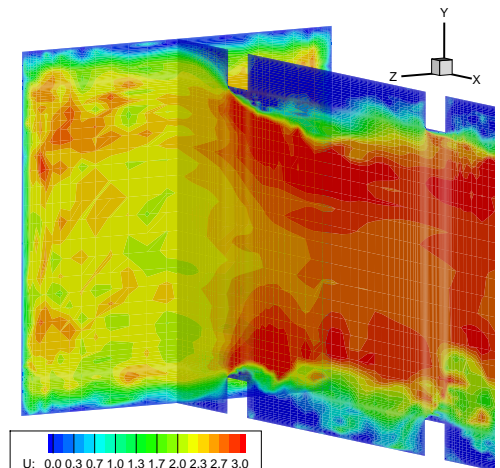
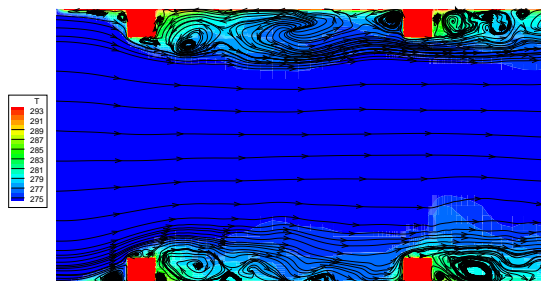


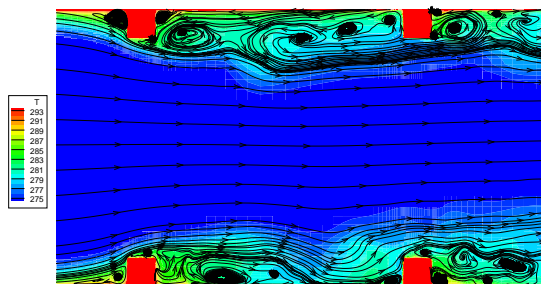
Figure 6: Turbulent duct flow imposed at the inlet.

Figure 7 shows temperature contours and streamlines with and without turbulence imposed at the inlet. The plane is located centrally in the span of the inlet leg. After the first rib, both flows display rapid development of large and small scales. Although the flow develops further downstream, inlet

turbulence does not appear to have a strong impact on flow development.



(a) With inlet turbulence



(b) Without inlet turbulence

Figure 7: Temperature field and streamlines near the inlet with and without inlet turbulence.

## 6. Results

### 6.1. Experimental data sources

Comparison is made with the aerodynamics and heat transfer data of [6] at a Reynolds number of 20,000, that of the current simulations. For heat transfer, which is more difficult to accurately predict, comparison is also made with the  $Re = 30,000$

data of [33] and [6]. The geometry of [33] is comparable ( $h/D = 0.1$  and  $D/h = 9$ ) with the current study ( $h/D = 0.1$  and  $D/h = 10$ ). The additional  $Re = 30,000$  data of [6] provides a comparison between the different experimental facilities. The two Reynolds numbers of Sewall also allow insight into any Reynolds number dependence. Overall, for heat transfer, there is approximately 10% difference between all experimental data sets. Initially, we will look at the flowfield.

### 6.2. Flow structure

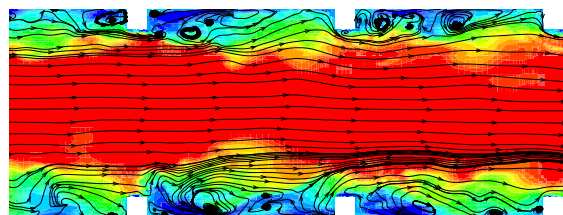


Figure 8: Instantaneous contours of streamwise velocity with streamlines for a section of the duct ( $3 \lesssim x/D \lesssim 5.5$ ).

Figure 8 shows a central spanwise plane in the inlet duct contoured with axial velocity. The flow can essentially be divided into two zones. The zone near the ribs (approximately  $2h - 3h$  from the outer walls) contains most turbulent activity. Around each rib small local recirculations persist and are

fairly stationary. Between the ribs, where the separated flow reattaches, the length of the recirculation bubble changes (by approximately  $0.3D$ ) as vortices are shed from the ribs and convected downstream. The movement of the reattachment point destroys most classical boundary layer content and locally increases heat transfer. The second zone is that of the core flow, where lower turbulence levels are observed and there is less mixing. This zone can be seen in red.

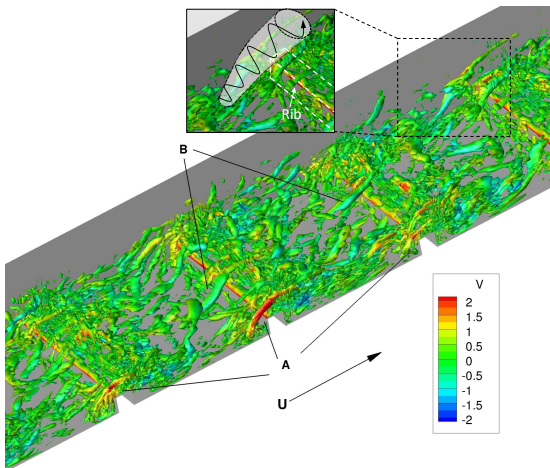


Figure 9: Iso-surface of the  $Q$ -criterion [34] coloured by  $v$ , with secondary flow diagram inset.

Figure 9 displays iso-surfaces of the  $Q$ -criterion ( $Q = \frac{1}{2}(|\Omega|^2 - |S|^2)$ , where  $\Omega$  and  $S$  define vorticity magnitude and strain rate respectively) [34]. This helps to identify coherent structures. The rib to sidewall junction

generates secondary flows. These are indicated by  $A$ . Also shown in the inset is an arrow showing the vortical motion produced. Recirculations can trap hot fluid at the rib junctions. In the centre of the duct, as indicated by  $B$ , large vortices are generated which rise over the ribs.

### 6.3. Mean flow and Turbulence statistics

Figure 10 shows mean axial velocity and mean fluctuating velocity components along the centerline of the inlet duct. All SGS models agree well with experimental data and there is little scatter between them. When no inlet turbulence is applied, most models show a small under-prediction in turbulence, but after approximately  $2D$ , agree well with data and only minor variations with SGS model are observed. This is also supported by Sewall [35], who finds fully developed flow after the second rib. When turbulence is applied at the inlet, the level of unsteadiness is initially too high, but again settles after around  $2 - 3D$ . As noted, two turbulence intensities are considered. Given the significant range of turbulence intensities, one of 0% and the other 10%, the flow seems insensitive to inlet turbulence due to rapid natural development.

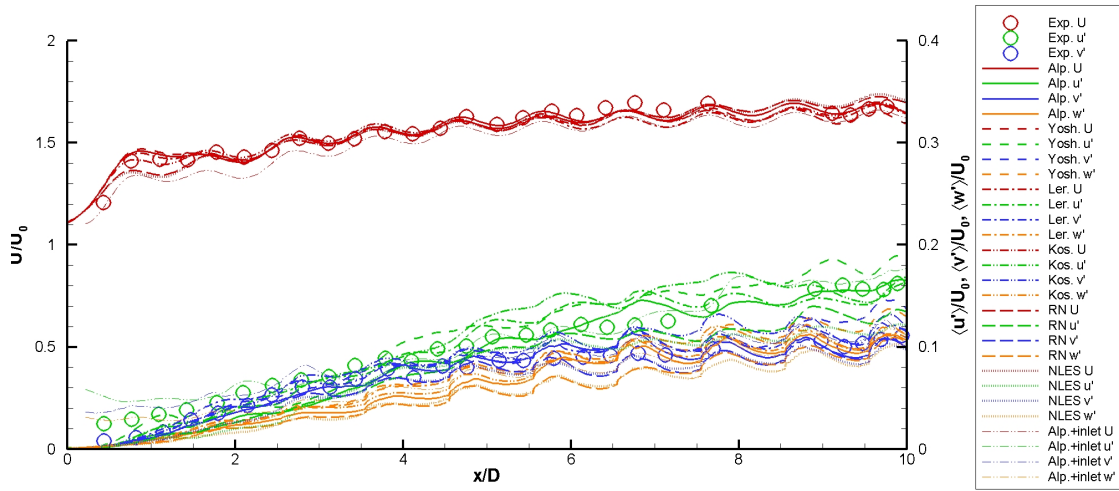
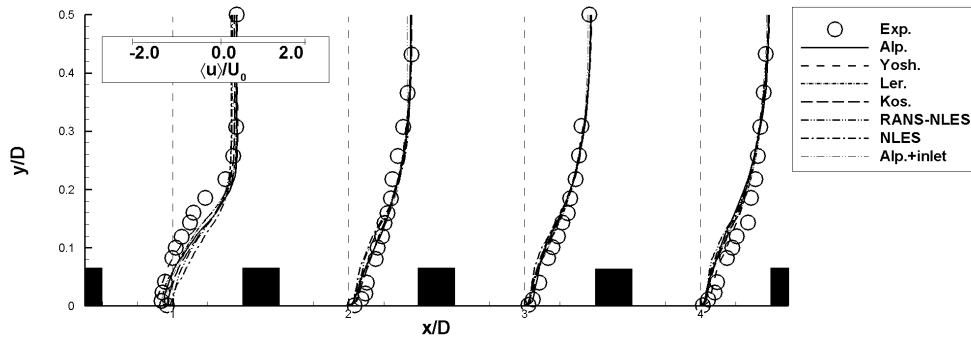
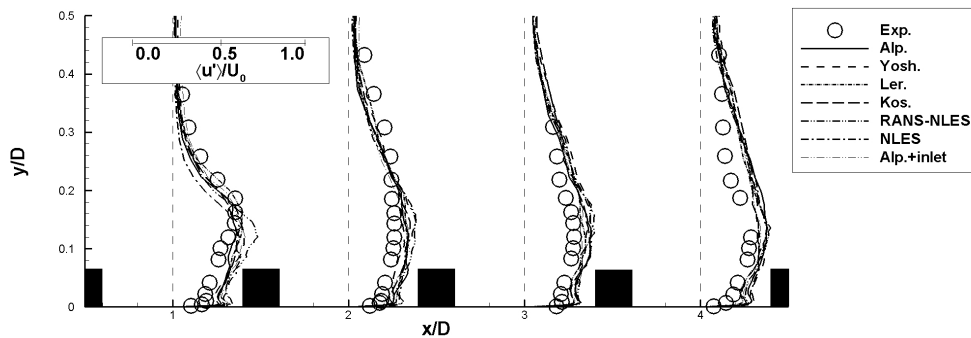


Figure 10: Developing mean and fluctuating velocity along the inlet duct centerline.

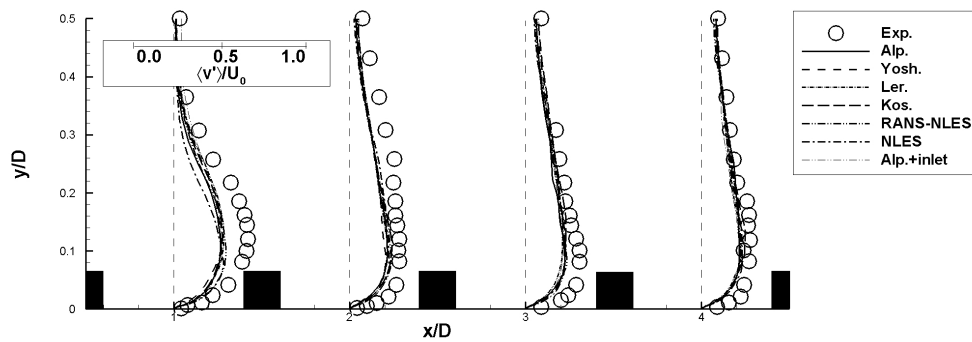


(a)

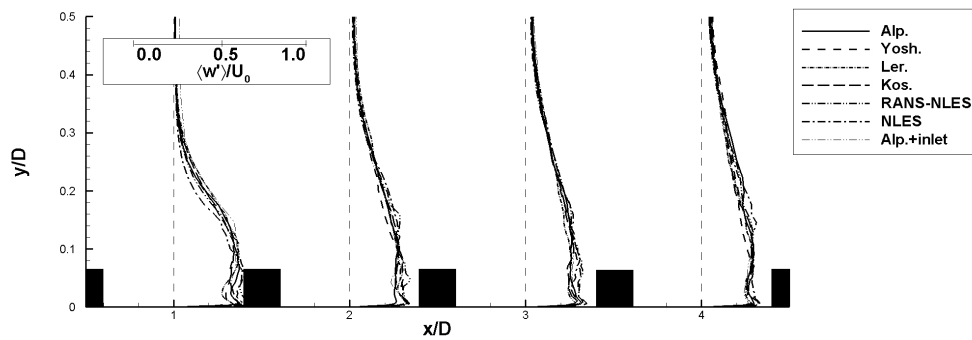


(b)

Figure 11: Flow quantities in the developing region of the duct: (a), mean streamwise velocity, (b), mean streamwise fluctuation.



(a)



(b)

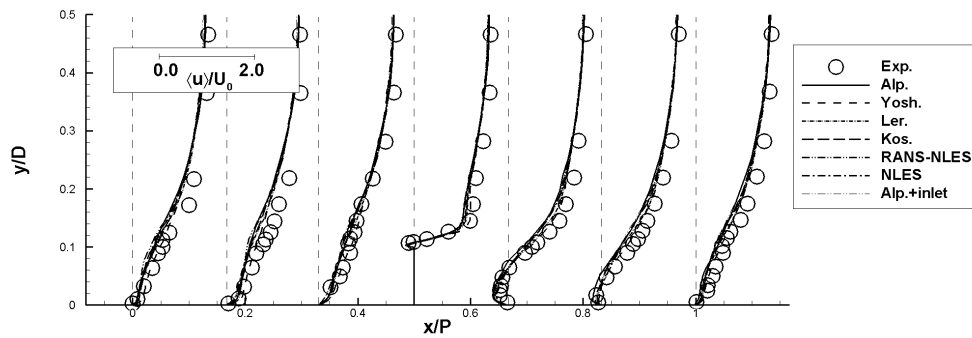
Figure 12: Flow quantities in the developing region of the duct: (a), mean vertical fluctuation, (b), mean spanwise fluctuation.

Figures 11–12 display vertical profiles taken at different  $x/D$  locations in the developing region of the duct. Figure 11a indicates that after the second rib ( $x/D = 2$ ), the mean axial velocity has reached a fully developed state, with all SGS models showing nearly identical profiles. The development of the RANS-NLES mean velocity also agrees well with the other LES profiles. This is in contrast to the DES [7] where DES delayed development. Shown in Fig. 11b are the mean streamwise fluctuation profiles. Again, profiles taken at  $x/D = 2 - 4$  are consistent. Figure 12a shows the vertical fluctuations, which although developed by the second rib, are slightly under-predicted within  $2h$  of the lower wall. Figure 12b displays the same trend for spanwise fluctuations. All profiles are in agreement with the available experimental data. Note, there is no experimental data available for the spanwise component.

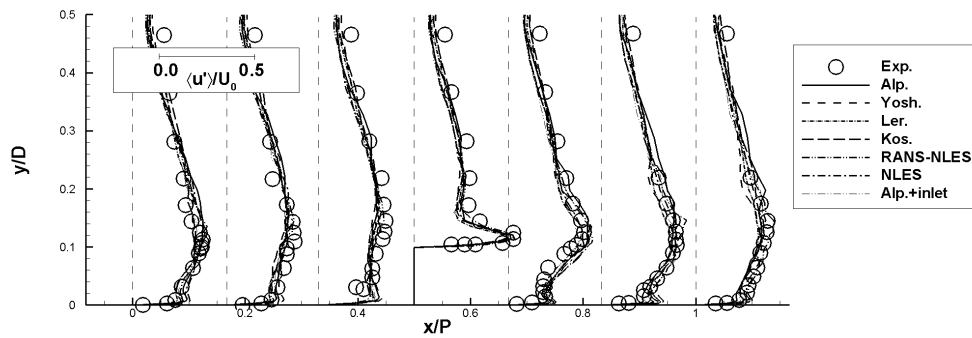
Flow quantities at several axial stations in a single rib pitch are displayed in Fig. 13 and 14. In Fig. 13a, the mean streamwise velocity profiles are again in agreement with experimental data throughout the rib pitch, with little variation with SGS model. Shown in Fig. 13b are the streamwise fluctua-

tions. Note agreement is also obtained near the wall downstream of the rib, where there is significant curvature in the profile. There is some variation with streamwise position but LES is in agreement with data. The vertical component shown in Fig. 14a shows little variation with streamwise position either side of the rib. The recirculations behind the ribs vary in length with time producing similar profiles along the pitch. Comparing with the streamwise profiles in Fig. 13b, most of the turbulence is generated within 1–2 rib heights. Fig. 14b highlights the substantial spanwise Reynolds stress component, again, with higher fluctuations near  $1 - 2h$ , where vortices are shed from the rib and convected both downstream and towards the centre of the duct.

Figure 15 displays the location of axial profiles of spanwise velocity at six vertical stations in the  $180^\circ$  bend. The corresponding velocity profiles are given in Fig. 16. In Fig. 16a, due to the complex turbulence production near the lower wall, some variation between the different SGS models can be seen. As in Fig. 16b–16f, as the profiles move outward from the lower wall, differences between models are mixed

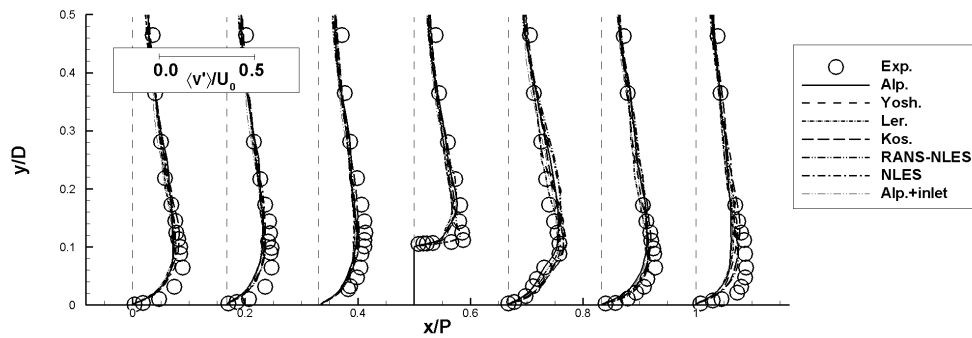


(a)

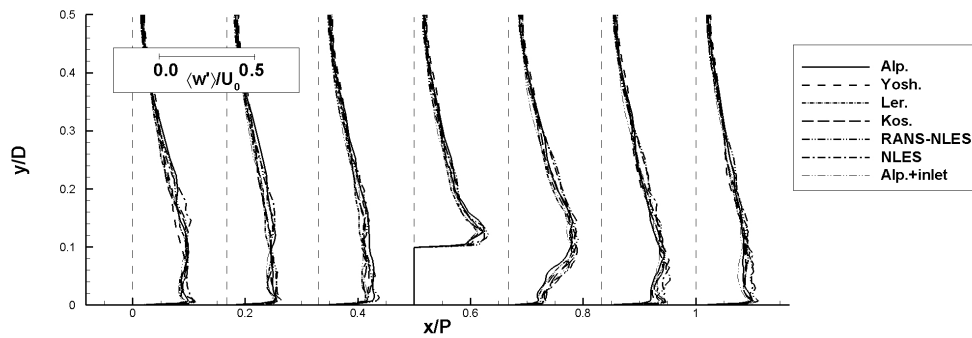


(b)

Figure 13: Flow quantities in one rib pitch of the duct: (a), mean streamwise velocity, (b), mean streamwise fluctuation.



(a)



(b)

Figure 14: Flow quantities in one rib pitch of the duct: (a), mean vertical fluctuation, (b), mean spanwise fluctuation.

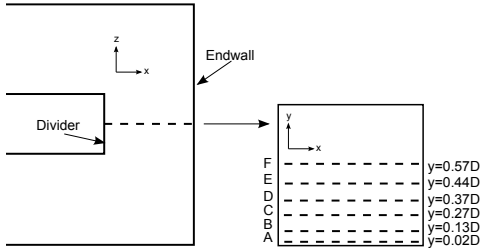


Figure 15: Schematic indicating spanwise profile locations.

out, the flow being dominated by large energy containing motions. The NLES and RANS-NLES may not provide enough overall dissipation (the code having low numerical dissipation) resulting in a small under-prediction near the channel centre. In contrast, the Yoshizawa model performs well. This is perhaps suggestive of the isotropic nature of wake-type flows, where large isotropic eddies are more amenable to linear modelling using a volumetric filter ( $\Delta = (\Delta x \Delta y \Delta z)^{1/3}$ ). Generally the non-linear models slightly improve results near walls, where higher anisotropy is found. Although small differences near the dividing and end walls cause some variation between SGS models, agreement with measurements is overall positive.

#### 6.4. Heat transfer

One of the most challenging aspects of modelling complex flows is that of heat

transfer. Figure 17 plots the Nusselt number distribution at the center of the bottom of the inlet duct (Fig. 17a). The quantity  $Nu/Nu_0$  indicates the heat transfer enhancement compared to that of flow over a flat plate. For all models, agreement with the measurements of [33] and [6] is observed. At each end of Fig. 17a there is some variation. This is due to the complex flow near the reattachment point. Figure 17a can be contrasted with Fig. 17b for a similar case modelled using linear and nonlinear RANS models [17]. There is a considerable range of results for different RANS turbulence models. Using LES, little reliance is placed on explicit turbulence models as 80-90% of turbulence is resolved.

A vertical profile  $0.5h$  upstream of the rib on the smooth side wall is also presented in Fig. 18 for the current LES. This again shows agreement with available measurements. It may be noted the measurements are not symmetrical in  $y$  suggesting potential skew in the flow altering computed errors. The measurements also show similar scatter to the LES in the region below  $2h$  making it hard to draw strong conclusions. In the center of the channel, models making use of NLES under-predict  $Nu$ , a small

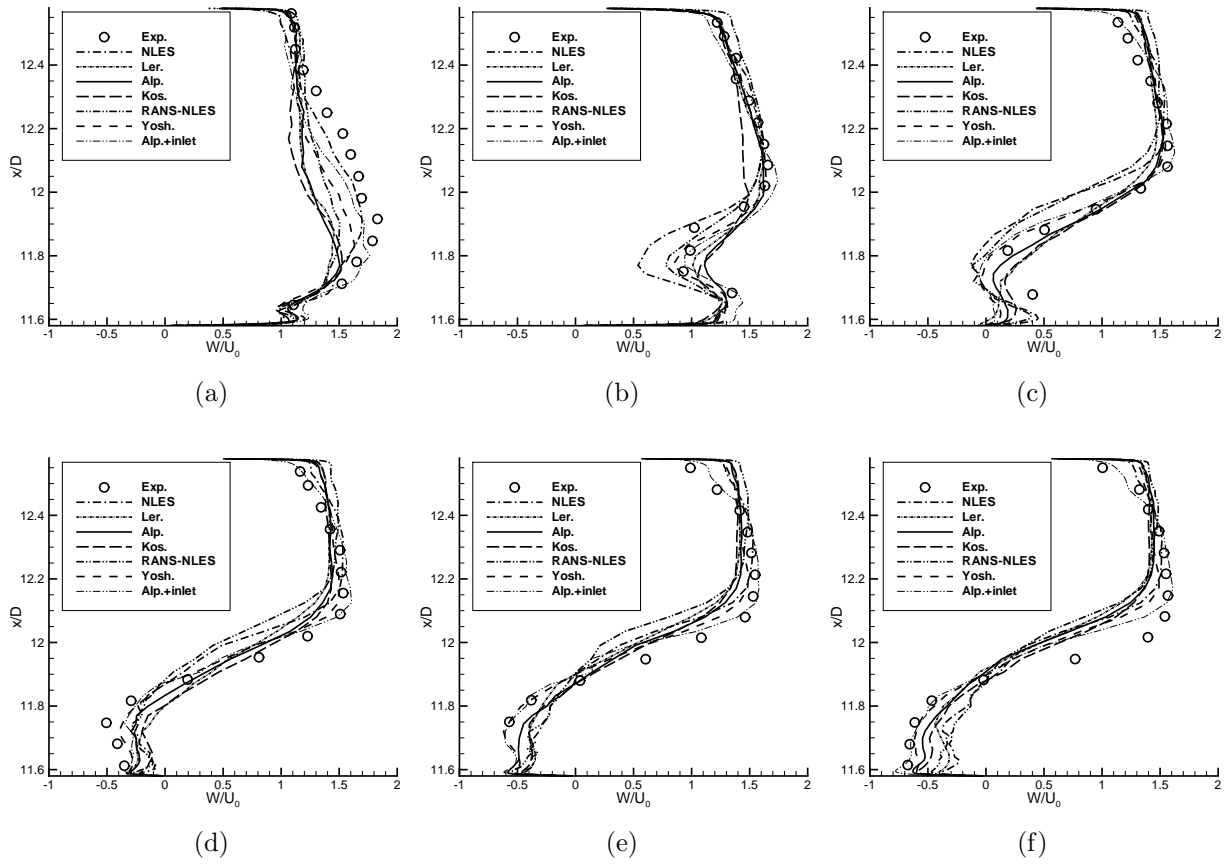


Figure 16: Axial profiles of mean spanwise velocity at six vertical stations A-F.

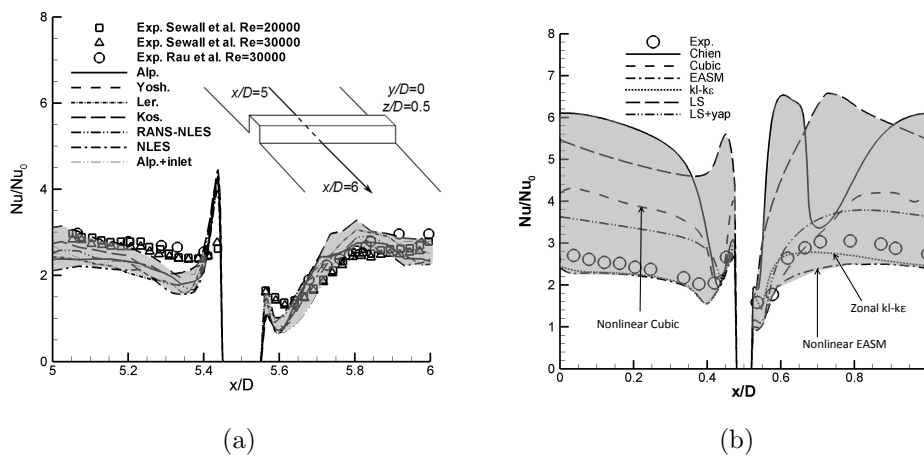


Figure 17: Nusselt number distribution: (a) across one rib pitch taken along the centre of the lower wall, (b) RANS results for a similar channel.

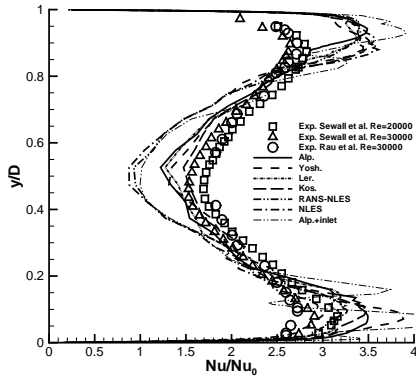


Figure 18: Nusselt number distribution - vertical profile on the smooth sidewall taken  $0.5h$  upstream of the rib.

benefit being gained from explicit SGS modelling. For both  $Nu$  plots, the Yoshizawa model performs well, perhaps being suited to more isotropic wake turbulence. Overall SGS models are consistent indicating SGS modelling has a low impact for these types of flows.

### 6.5. Anisotropy Invariant Maps

To show graphically the difference in turbulence structure, Anisotropy Invariant Maps (AIMs) can be plotted. Figure 19a indicates the different states of the turbulent stress anisotropy using the second and third Reynolds stress invariants represented by  $\eta$  and  $\xi$  respectively (see [36, 14]). All realisable states of the turbulent stress tensor lie within the triangle formed [36]. Plot-

ting the second and third invariants along a profile provides a map of how the different stress components change relative to each other, indicating the direction and magnitude of the different stresses along that profile. For typical boundary layer flows, the upper right 1D region indicates the elongated near wall streaks, the lower middle represents 3D isotropic stresses. Further details can be found in [37]. Hence with knowledge of the flow, the nature of the turbulent stresses can be identified, particularly whether the turbulent stresses being modelled are isotropic or not. Figure 19b plots an AIM for the Alpha model including inlet turbulence along a profile at  $x/P = 1, z/D = 0.5$  used in Figs. 13 and 14). Figure 19c plots the same profile but at  $z = 0.5h$ . The change in line colour approximates the path from the lower to upper walls (i.e.  $0 < y/D < 1$ ).

In the centre of the duct (Fig. 19b), the stresses begin at the duct floor as 2D moving towards 2D isotropic. Towards the duct centre, the stresses become more cigar shaped. Similar shaped vortices can be seen in Fig. 9. Nearer the outer wall, the stresses are between the cigar-shaped and 1D turbulence zones. This indicates higher

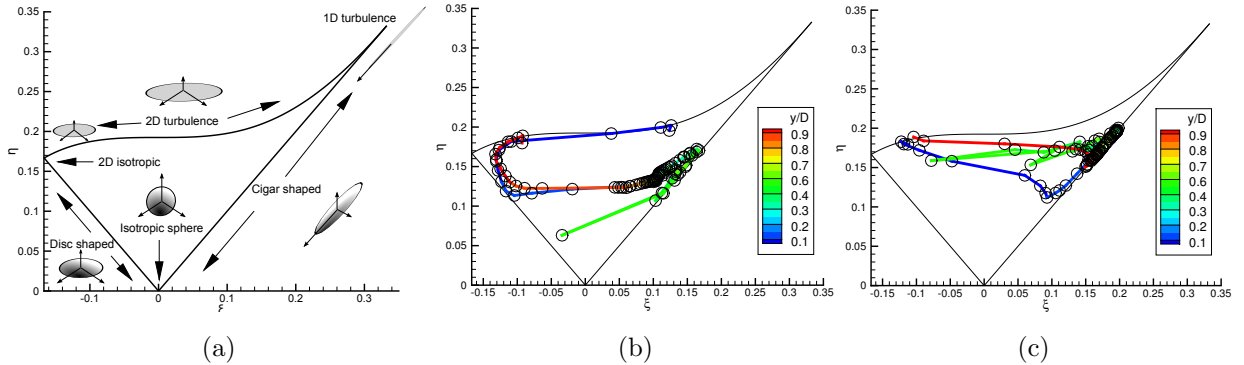


Figure 19: (a) AIM diagram indicating the possible state of stresses. AIM for a profile in a single rib pitch: (b), centre of the inlet duct, (c),  $0.5h$  from the outer wall of the inlet duct.

anisotropy due to multiple walls and straining, with a small amount of 2D activity near the top and bottom walls. This stress anisotropy may explain to some extent the partial success of RANS modelling for 2D ducts (most like the duct centre) and failure for more complex 3D flows.

### 6.6. Results summary

Table 2: Average errors (%) for extracted profiles.

Model	$\langle u \rangle$ and $\langle w \rangle$	$\langle u' \rangle$ and $\langle v' \rangle$	$Nu$
Yosh.	3.2	5.4	12.3
Ler.	4.3	5.2	16.2
Alp.	4.1	5.4	15.8
Kos	4.2	5.1	15.7
NLES	4.8	5.7	19.1
RANS-NLES	5.3	5.6	18.1
Alp. + inflow	3.7	5.3	19.2
Average	4.2	5.3	16.9

Table 2 provides average errors for each SGS model. Errors are provided for mean velocities  $\langle u \rangle$  and  $\langle w \rangle$ , mean velocity fluctuations  $\langle u' \rangle$  and  $\langle v' \rangle$  and heat transfer  $Nu$  and are averaged over all extracted profiles to provide an overview of results. Errors are calculated using Eq. 10 below, for velocities and heat transfer from [6].

$$\frac{\sum_{n=1}^{n_{exp}} |\phi_{exp} - \phi_{num}|}{\sum_{n=1}^{n_{exp}} U_0}, \quad \frac{\sum_{n=1}^{n_{exp}} |Nu_{exp} - Nu_{num}|}{\sum_{n=1}^{n_{exp}} Nu_{exp}} \quad (10)$$

Here, *exp* and *num* refer to experimental and numerical data points. Where numerical data points do not coincide with experiments, a stiff quadratic spline is used to interpolate. Errors are similar to those of [18, 5] who obtain errors within 10-20%.

As shown in Tab. 2, the average errors for all variables do not vary significantly between different SGS models, however some comments can be made. The NEAT solver is neutrally dissipative [15], hence overall, the more dissipative Yoshizawa and mixed nonlinear LES models perform the best, as shown by Tab. 2. These introduce dissipation through the linear subgrid viscosity terms, which may be required to drain energy from the large scales that the grid is designed for. The flow in the critical zone of interest is not expected to develop fine near wall structures, such as those found in boundary layer-type flows, due to the flow separation and reattachment near the rib mid-pitch. The models based on NLES lack the additional dissipative element related to the subgrid scales, hence the near wall RANS layer in the RANS-NLES slightly improves predictions but does not dominate the flow, supporting the notion that the near wall region is not dominated by classical boundary layer type flow. If this had been the case, dramatic differences would have been observed. For example, Tucker et al. [38] display this with compressor end-wall flow. Other industrial solvers that use more dissipative numerical schemes may in-

deed find that an explicit SGS model is not required, particularly compressible flow solvers, which may also introduce additional dissipation near walls in low Mach regions [39]. It is hence important that SGS models are chosen that suit the solver numerics being used to avoid double accounting of the SGS scales and excessive dissipation [40].

To compare the overall reliability of RANS and LES modelling, Tab. 3 provides the mean error and standard deviation for heat transfer, as displayed in Fig. 17. These are averaged across all turbulence models employed for RANS and (N)LES-based (those with (N)LES content including hybrid RANS-NLES) simulations. The mean error for RANS is significantly higher than that of (N)LES. Even more stark is the contrast between the standard deviation. Large scale unsteadiness and strong streamline curvature makes the reliable use of RANS for heat transfer challenging. This is mainly due to the linear eddy-viscosity models, the nonlinear models such as the Cubic and EASM indicated in Fig. 17b show some improvement. Clearly picking a suitable SGS model is not as critical as when using RANS. This type of flow is highly suited to LES and the use of Immersed Boundary

Table 3: Mean and standard deviation (%) for RANS and (N)LES-based heat transfer.

	RANS	(N)LES-based	Factor (RANS:(N)LES-based)
Mean error (%)	48.4	16.9	2.9
Std. Dev. (%)	37.5	2.2	17.0

Methods [41] due to the large scales generated. Unlike RANS, LES will not be as sensitive to different rib-topologies or the inclusion of rotation effects as these will be resolved in space and time. This indicates ribbed internal cooling ducts may be one of the first practical industrial applications for LES.

## 7. Conclusions

Flow and heat transfer predictions are compared with measurements and found to be in excellent agreement considering the relatively small grid. The choice of LES model is found to be of minor importance as the flow is dominated by large geometric scale structures. The influence of inlet turbulence is also tested and has a minor impact due to the strong turbulence generated by the ribs. This is in contrast to linear RANS models, which are shown to perform poorly for heat transfer. For LES, large scale turbulent motions destroy any classical boundary layer reducing near wall grid

requirements. The wake-type flow structure makes this and similar flows nearly Reynolds number independent allowing a range of flows to be studied at similar cost. Hence LES is a relatively cheap method for obtaining accurate heat transfer predictions in these types of flows.

## References

- [1] A. Ooi, G. Iaccarino, P. Durbin, M. Behnia, Reynolds averaged simulation of flow and heat transfer in ribbed ducts, *International Journal of Heat and Fluid Flow* 23 (6) (2002) 750–757. doi:10.1016/S0142-727X(02)00188-1.
- [2] J. C. Tyacke, Low Reynolds number heat transfer prediction employing Large Eddy Simulation for electronics geometries, Ph.D. thesis, Civil and Computational Engineering Centre, Swansea University (2009).
- [3] A. K. Saha, S. Acharya, Flow and Heat Transfer in an Internally Ribbed Duct With Rotation: An Assessment of Large Eddy Simulations and Unsteady Reynolds-Averaged Navier-Stokes Simulations, *Journal of Turbomachinery* 127 (2) (2005) 306. doi:10.1115/1.1861917.
- [4] M. Germano, U. Piomelli, P. Moin, W. H.

- Cabot, A dynamic subgrid-scale eddy viscosity model, *Physics of Fluids A: Fluid Dynamics* 3 (7) (1991) 1760–1765. doi:10.1063/1.857955.
- [5] D. K. Tafti, Evaluating the role of subgrid stress modeling in a ribbed duct for the internal cooling of turbine blades, *International Journal of Heat and Fluid Flow* 26 (2005) 92–104.
- [6] E. A. Sewall, D. K. Tafti, A. B. Graham, K. A. Thole, Experimental validation of large eddy simulations of flow and heat transfer in a stationary ribbed duct, *International Journal of Heat and Fluid Flow* 27 (2) (2006) 243–258. doi:10.1016/j.ijheatfluidflow.2005.08.010.
- [7] A. K. Viswanathan, D. K. Tafti, Detached eddy simulation of turbulent flow and heat transfer in a two-pass internal cooling duct, *International Journal of Heat and Fluid Flow* 27 (1) (2006) 1–20. doi:10.1016/j.ijheatfluidflow.2005.07.002.
- [8] P. R. Spalart, W.-H. Jou, M. Strelets, S. R. Allmaras, Comments on the feasibility of LES for wings, and on a hybrid RANS/LES approach, First AFOSR International Conference on DNS/LES in *Advances in DNS/LES* (1997) 137–147.
- [9] A. G. Ramgadia, A. K. Saha, Large Eddy Simulation of Turbulent Flow and Heat Transfer in a Ribbed Coolant Passage, *Journal of Applied Mathematics* 2012 (2012) 1–21. doi:10.1155/2012/246313.
- [10] P. G. Tucker, *Unsteady Computational Fluid Dynamics in Aeronautics*, Springer, 2013.
- [11] S. Kunstmann, *Heat Transfer and Pressure Loss in Rectangular One-Side-Ribbed Channels With Different Aspect Ratios*, *Journal of Turbomachinery* 135 (3) (2013) 031004. doi:10.1115/1.4006871.
- [12] P. Promvong, W. Changcharoen, S. Kwankaomeng, C. Thianpong, Numerical heat transfer study of turbulent square-duct flow through inline V-shaped discrete ribs, *International Communications in Heat and Mass Transfer* 38 (10) (2011) 1392–1399. doi:10.1016/j.icheatmasstransfer.2011.07.014.
- [13] J. C. Han, Y. M. Zhang, High performance heat transfer ducts with parallel broken and V-shaped broken ribs, *Int. J. Heat Mass Transfer* 35 (2) (1992) 513–523.
- [14] S. B. Pope, *Turbulent Flows*, Cambridge University Press, 2000.
- [15] P. G. Tucker, *Computation of Unsteady Internal Flows*, Kluwer Academic Publishers, 2001.
- [16] S. V. Patankar, *Numerical Heat Transfer and Fluid Flow*, Series in computational methods in mechanics and thermal sciences, Taylor & Francis, 1980.
- [17] J. Tyacke, P. Tucker, LES of heat transfer in electronics, *Applied Mathematical Modelling* 36 (7) (2012) 3112–3133. doi:10.1016/j.apm.2011.09.072.
- [18] E. A. Sewall, D. K. Tafti, Large Eddy Simulation of Flow and Heat Transfer in the Developing Flow Region of a Rotating Gas Turbine Blade Internal Cooling Duct With Coriolis and Buoyancy Forces, *Journal of Turbomachinery* 130 (1) (2008) 011005. doi:10.1115/1.2437779.
- [19] A. Yoshizawa, Bridging between eddy-

- viscosity-type and second-order models using a two-scale DIA, In: Proceedings of the 9th International Symposium on Turbulent Shear Flow, Kyoto 3 (0) (1993) 1–23.
- [20] L. Davidson, S. H. Peng, Hybrid LES-RANS modelling: a one-equation SGS model combined with a  $k-\omega$  model for predicting recirculating flows, *International Journal for Numerical Methods in Fluids* 43 (9) (2003) 1003–1018.
- [21] M. Wolfshtein, The velocity and temperature distribution in one-dimensional flow with turbulence augmentation and pressure gradient, *International Journal of Heat and Mass Transfer* 12 (3) (1969) 301–318.
- [22] J. A. Domaradzki, W. Liu, M. E. Brachet, An analysis of subgrid-scale interactions in numerically simulated isotropic turbulence, *Phys. Fluids* 41 (1993) 453–480.
- [23] B. J. Geurts, D. Holm, Leray and LANS- $\alpha$  modelling of turbulent mixing, *Journal of Turbulence* 0 (2005) 1–42.
- [24] P. Sagaut, *Large Eddy Simulation for Incompressible Flows: An Introduction*, 3rd Edition, Scientific Computation, Springer, 2006.
- [25] J. Smagorinsky, General circulation experiments with the primitive equations. I. The basic experiment, *Monthly Weather Review* 91 (3) (1963) 99–165.
- [26] D. Drikakis, M. Hahn, A. Mosedale, B. Thornber, Large Eddy Simulation Using High Resolution and High Order Methods, *Phil. Trans. R. Soc. A* 367 (2009) 2985–2997.
- [27] F. Grinstein F., C. Fureby, R. DeVore C., On MILES based on flux-limiting algorithms, *International Journal for Numerical Methods in Fluids* 47 (10-11) (2005) 1043–1051.
- [28] P. G. Tucker, Y. Liu, Contrasting a novel temporally oriented Hamilton-Jacobi-equation-based ILES method with other approaches for a complex geometry flow, *International Journal for Numerical Methods in Fluids* 48 (11) (2005) 1241–1257.
- [29] Y. Liu, P. G. Tucker, G. Lo Iacono, Comparison of zonal RANS and LES for a non-isothermal ribbed channel flow, *International Journal of Heat and Fluid Flow* 27 (2006) 391–401.
- [30] W. P. Jones, B. E. Launder, E. Road, The calculation of low-Reynolds-number phenomena with a two-equation model of turbulence, *Int. J. Heat Mass Transfer* 16 (1973) 1119–1130.
- [31] S. Vodret, D. V. Di Maio, G. Caruso, Numerical simulation of turbulent forced convection in liquid metals, *Journal of Physics: Conference Series* 547 (2014) 012033. doi:10.1088/1742-6596/547/1/012033.
- [32] A. Graham, E. Sewall, K. A. Thole, Flowfield Measurements in a Ribbed Channel Relevant to Internal Turbine Blade Cooling, in: *ASME Turbo Expo 2004*, 2004.
- [33] G. Rau, M. Çakan, D. Moeller, T. Arts, The Effect of Periodic Ribs on the Local Aerodynamic and Heat Transfer Performance of a Straight Cooling Channel, *Journal of Turbomachinery* 120 (2) (1998) 368–375. doi:10.1115/1.2841415.
- [34] J. C. R. Hunt, A. A. Wray, P. Moin, Eddies, streams, and convergence zones in tur-

- bulent flows, in: Center for Turbulence Research, Vol. 1, Center for Turbulence Research, Center for Turbulence Research, NASA Ames/Stanford Univ., 1988, pp. 193–208.
- [35] E. A. Sewall, Large Eddy Simulations of Flow and Heat Transfer in the Developing and 180 Bend Regions of Ribbed Gas Turbine Blade Internal Cooling Ducts with Rotation - Effect of Coriolis and Centrifugal Buoyancy Forces, Phd, Virginia Polytechnic Institute and State University (2005).
- [36] J. Lumley, Computational modelling of turbulent flows, *Adv. Appl. Mech.* 18 (1978) 123–176.
- [37] a. J. Simonsen, P.-a. Krogstad, Turbulent stress invariant analysis: Clarification of existing terminology, *Physics of Fluids* 17 (8) (2005) 088103. doi:10.1063/1.2009008.
- [38] P. Tucker, S. Eastwood, C. Klostermeier, H. Xia, P. Ray, J. Tyacke, W. Dawes, Hybrid LES Approach for Practical Turbomachinery Flows: Part 2 - Further Applications, *ASME Conference Proceedings (44021)* (2010) 1055–1067. doi:10.1115/GT2010-23807.
- [39] J. M. Weiss, W. A. Smith, Preconditioning Applied to Variable and Constant Density Flows, *AIAA Journal* 33 (11) (1995) 2050–2057.
- [40] N. J. Georgiadis, D. P. Rizzetta, C. Fureby, Large-Eddy Simulation : Current Capabilities , Recommended Practices , and Future Research, *AIAA Journal* 48 (8) (2009) 1772–1784.
- [41] C. S. Peskin, Flow patterns around heart valves: A numerical method, *Journal of Computational Physics* 10 (1972) 252–271. doi:10.1016/0021-9991(72)90065-4.